

A Study of the Failure Mechanism of Planar Non-Persistent Open Joints Using PFC2D

A. Ghazvinian · V. Sarfarazi · W. Schubert ·
M. Blumel

Received: 29 November 2011 / Accepted: 19 February 2012 / Published online: 17 March 2012
© Springer-Verlag 2012

Abstract Particle flow code 2D (PFC2D) was adopted to simulate the shear behavior of rocklike material samples containing planar non-persistent joints. Direct shear loading was conducted to investigate the effect of joint separation on the failure behavior of rock bridges. Initially calibration of PFC was undertaken with respect to the data obtained from experimental laboratory tests to ensure the conformity of the simulated numerical models response. Furthermore, validation of the simulated models were cross checked with the results of direct shear tests performed on non-persistent jointed physical models. Through numerical direct shear tests, the failure process was visually observed, and the failure patterns were found reasonably similar to the experimentally observed trends. The discrete element simulations demonstrated that the macro-scale shear zone resulted from the progressive failure of the tension-induced micro-cracks. The failure pattern was mostly influenced by joint separation, while the shear strength was linked to the failure pattern and failure mechanism. Furthermore, it was observed that the failure zone is relatively narrow and has a symmetrical pattern when rock bridges occupy a low percentage of the total shear surface. This may be due to the

high stress interactions between the subsequent joints separated by a rock bridge. In contrast, when rock bridges are occupying sufficient area prohibiting the stress interactions to occur then the rupture of surface is more complex and turns into a shear zone. This zone was observed to be relatively thick with an unsymmetrical pattern. The shear strength of rock bridges is reduced by increasing the joint length as a result of increasing both the stress concentration at tip of the joints and the stress interaction between the joints.

Keywords Particle flow code · Non-persistent joint · Rock bridge · Joint separation · Shear and tensile cracks

1 Introduction

The behavior of a rock mass is determined not only by the properties of the rock matrix, but mostly by the presence and properties of discontinuities within the mass. The different kinds and origins of discontinuities play a dominant role in the failure of rock mass (Tang et al. 1998; Wong and Chau 1998).

The initiation, propagation and coalescence of rock cracks are important factors in controlling the mechanical behavior of brittle rocks. Crack propagation and coalescence can reduce the stiffness of jointed rock masses causing the shear failure of rock slopes (Einstein et al. 1983).

Therefore, a comprehensive study on the shear failure behavior of non-persistent joints can provide a good understanding of both local and general rock instability, leading to an improved design for rock engineering projects.

From another point of view, extra financial charges are levied on the rock engineering projects as the supportive action of the rock bridges is being neglected by the

A. Ghazvinian (✉) · V. Sarfarazi
Rock Mechanics Division, Tarbiat Modares University,
Tehran, Iran
e-mail: Hadi@modares.ac.ir

V. Sarfarazi
e-mail: Vahab.sarfarazi@gmail.com

W. Schubert · M. Blumel
Institute for Rock Mechanics and Tunnelling,
Graz University of Technology, Graz, Austria
e-mail: Schubert@tugraz.at

M. Blumel
e-mail: Blumel@tugraz.at

designers in actual projects. This research is intended to contribute to and highlight such effects as far as possible within the frame of the planned research work.

The failure behavior of jointed rock masses under shear loading has drawn ample attention from both researchers and practical engineers over the last 3 decades, and some extensive works on the coalescence pattern and shear resistance of non-persistent joints have been carried out through a large number of experimental and theoretical studies. In one of the pioneering works done by Lajtai (1969a, b), tensile wing cracks were found to first appear at the tips of horizontal joints, followed by the secondary shear cracks propagating towards the opposite joints. Ghazvinian et al. (2007) prepared a comprehensive analysis of the shear behavior of rock bridges based on the change in the persistence of their area. The analysis showed that the failure mode and mechanism were affected by the continuity of the rock bridges.

Although some promising results on the specimens containing non-persistent open joints in different geometry conditions under shear loading have been obtained, the whole failure process from crack initiation, propagation and coalescence to failure is not yet clear. The fracture of synthetic brittle materials is so violent that it is difficult to trace the whole failure process from crack initiation, propagation and coalescence by the existing limited monitoring devices (Glynn et al. 1978). Also the experimental results are very sensitive to sample preparation processes and the boundary loading conditions; thus any small change in the contact condition between the sample and loading platen may result in different failure modes for the sample. A numerical approach appears to be necessary for studying crack propagation and coalescence in rock because of the mechanical and geometrical complexity of most of the related problems.

Some important work has been carried out on the numerical simulations on crack propagation and coalescence in multiple cracks. Using the displacement discontinuity method (DDM), Scavia and Castelli (1996) and Scavia (1999) have conducted some preliminary work to investigate the mechanical behavior of rock bridges in the material containing two and three crack-like flaws. A series of numerical analyses were carried out to evaluate the influence of overlapping so as to identify a critical value of the resistance of the rock bridge. The results revealed that tensile crack propagation occurs in either stable or unstable conditions depending on the flaw spacing and applied confining stresses. Vasarhelyi and Bobet (2000) have used DDM to model the crack initiation, propagation and coalescence between the two bridged flaws in gypsum under uniaxial compression. Their simulations reproduced the types of coalescence observed in the experiments and predicted an increase in the coalescence stresses with

ligament length. While a good agreement between the numerical and experimental results was found as for the propagation trajectory of the tensile and shear cracks in the numerical models containing multiple flaws, a few numerical models have been found to be able to simulate the shear response of the specimens containing non-persistent joint under direct shear.

The discrete element method (DEM) is also another capable method for studying the failure behavior of bonded geomaterials (Potyondy and Cundall 2004; Fakhimi et al. 2002; Wang and Tannant 2004; Hentz et al. 2004; Yoon 2004).

In this study, the particle flow code in two dimensions (PFC2D), which is a program based on the principle of DEM, was used as the simulation platform to investigate the effect of joint separation on the shear behavior of rock bridges. Therefore, concurrent with experimental investigation of shear behavior of non-persistent joints, it is possible to check the ability of DEM in determining failure patterns in rock bridges by comparison of the numerical and experimental results.

First, the laboratory experiments were performed to calibrate the intact rock micro-mechanical parameters. Using an inverse-modeling calibration approach, the laboratory results of the uniaxial, Brazilian and triaxial tests were used to obtain the estimates of the intact rock micro-mechanical parameters used in the simulation. A validation of the simulation was then performed by comparison between the shear behavior of rock bridges in PFC2D and that of the non-persistent joint tested under direct shear loading in the laboratory. The validated numerical model was used to further studying the mechanical behavior of the jointed models with different joint persistency.

2 Laboratory Tests

2.1 Model Material Preparation

The model material used in preparing the intact samples and jointed blocks was a mixture of plaster (37.5 %), cement (25 %) and water (37.5 %).

The mixing, casting and curing of the specimens were carefully controlled to obtain reproducible properties. Mixing of the material constituents was carried out with a blender. To ensure the maximum possible homogeneity and isotropy of the overall compound, the plaster and the cement were mixed together prior to the addition of water. Then, water was added to the dry mix of the constituents and thoroughly re-mixed. The mixed material was hardened in about 10 min. This means that thorough mixing needs to be done quickly to obtain a homogeneous mixture. The mixed material was cast in different shapes and

volumes to prepare samples for different types of laboratory testing. The samples were then removed from the mold and kept in the geo-mechanics laboratory room with the temperature controlled at 20 ± 2 °C for a fixed number of days (20 days) before being subjected to mechanical testing.

The cylindrical sample mold dimensions were 54 mm in diameter and 108 mm in length, and the disc sample mold dimensions 54 mm in diameter and 27 mm in thickness (Fig. 1a).

2.2 Intact Model Material Properties

The uniaxial, triaxial compression and Brazilian tensile tests were performed in the Rock Mechanics Laboratory of Graz University of Technology, Graz, Austria, by their Machine Tool System (MTS) in order to determine the mechanical properties of the intact model material. The mechanical properties of the physical models are summarized in Table 1.

2.3 Preparation, Testing and Results of the Models Consisting of Non-Persistent Joints

The procedure developed by Bobet and Einstein (1998) for preparing open non-persistent joints was used in this research with some modifications. The mold's dimensions for discontinuous jointed samples were 190 mm in length, 150 mm in width and 50 mm in thickness. The mold consisted of four 20-mm-thick fiberglass sheets bolted together plus two fiberglass plates (placed at the top and bottom of the mold) (Fig. 1b). The top plate has two orifice openings used to fill the mold with the liquid mixture. The upper and the lower surfaces have slits cut into them. The opening of the slits is 1 mm, and their tract is equal to the width of the model. Through these slits, greased metallic

shims are inserted through the thickness of the mold (to produce non-persistent joints) before pouring of the gypsum. Each sample was kept in the mold for about 7 h, the specimens were un-molded, and the metallic shims were pulled out of the specimens. The grease on the shims prevents adhesion of the shim with the sample and facilitates the removal of the shims. As the mixture is placed and hardened, each shim leaves an open joint in the specimen through the thickness and perpendicular to the front and back of the specimen. It appears that the pulling out of the shims does not produce any damage to the joints. Immediately after removing of the shims, the specimen is stored in the laboratory room with the temperature controlled at 20 ± 2 °C for 20 days. It is important to note that consistency in mixing, casting, curing and testing is required to obtain acceptable test results.

Two specimens with different ligament lengths of 45 mm and 90 mm were prepared. (Ligament length is the distance between the tips of two joints (Fig. 2a).)

A servo-controlled MTS direct shear apparatus, shown in Fig. 2b, was used for the purpose of testing the artificial non-persistent joints. All samples were tested by applying a shear displacement rate of 0.01 mm/s. The normal stress applied to the rock bridges was 0.33 MPa, which is approximately 5 % of the uniaxial strength of intact sample. The shear loads as well as the shear displacements were taken by a data acquisition system during the shear test.

The crack pattern was observed after completion of the test. It was observed that the pre-existing joint surfaces have not been destroyed during the test. It means that the rock joint has no effect on the shear behavior of the rock bridge. The shearing process of a discontinuous joint constellation begins, as one would expect, with the formation of new fractures, which eventually transect the material bridges and lead to a through-going discontinuity. The observation results showed that the ligament length

Fig. 1 a Two different molds used for fabrication of the cylindrical samples, b the mold used for fabrication of the jointed specimens

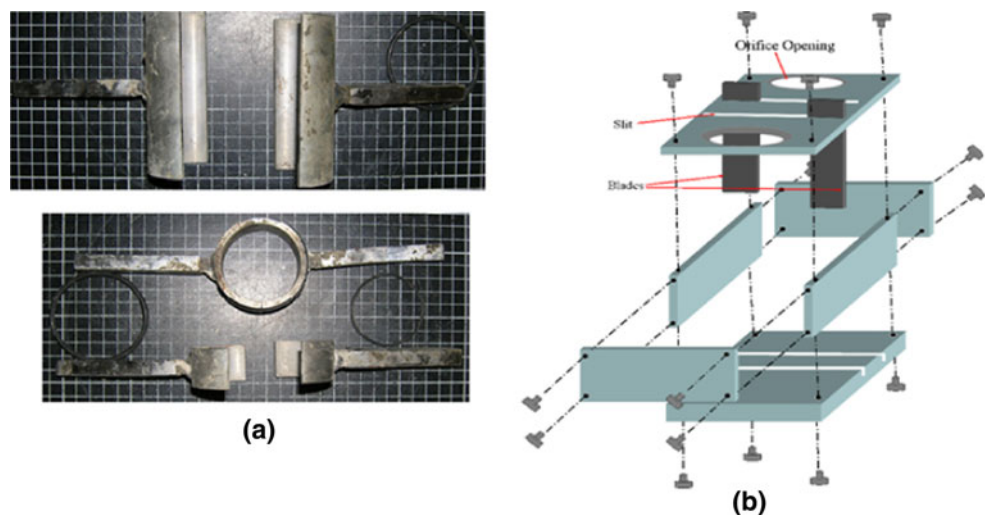


Table 1 Property values of the intact model material determined experimentally

Property	Value
Average uniaxial compressive strength (MPa)	6.6
Average Brazilian tensile strength (MPa)	1
Average Young's modulus in compression (GPa)	5
Average Poisson's ratio	0.18
Internal angle of friction	20.4°
Cohesion (MPa)	2.2

influences the failure pattern of the rock bridge. Figure 3 shows two different types of failure pattern obtained in the direct shear tests.

- When the ligament length is 45 mm (Fig. 3a), the upper tensile crack propagates through the intact portion area, but the lower tensile crack develops for a short distance and then becomes stable and does not coalesce with the tip of the other joint.
- When the ligament length is 90 mm (Fig. 3b), the interaction between the joints is not strong so that the tensile crack propagates in the mid zone. Thus, the rock bridge is broken with an uneven failure surface.

In these failure patterns, the surface of failure at the bridge area is tensile because no crushed or pulverized materials were noticed.

3 Numerical Modeling with PFC

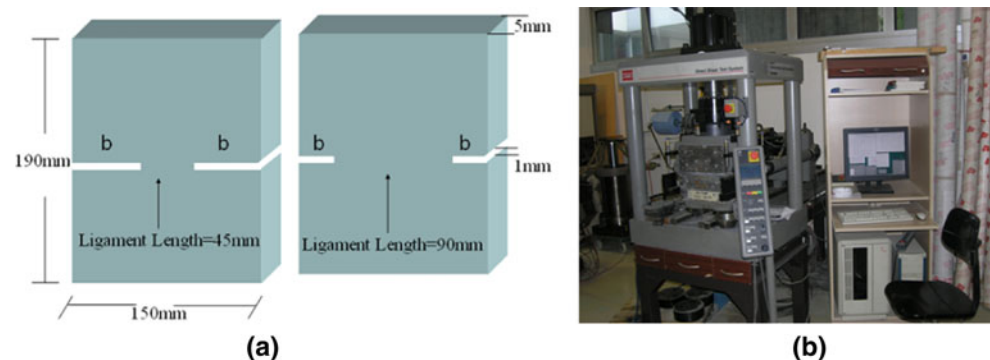
Discrete element modeling (DEM) is now often used to simulate the behavior of rock (Potyondy and Cundall 2004). The method is attractive because it does not require the formulation of complex constitutive models (Cundall 1971).

Particle flow code represents a rock mass as an assemblage of bonded rigid particles. In the two-dimensional version (PFC2D), circular disks are connected with cohesive and frictional bonds and confined with planar walls.

The parallel bond model was adopted in this study to simulate the contacts between the particles. The values assigned to the strength bonds influence the macro strength of the sample and the nature of cracking and failure that occurs during loading. Friction is activated by specifying the coefficient of friction and is mobilized as long as particles stay in contact. Tensile cracks occur when the applied normal stress exceeds the specified normal bond strength. Shear cracks are generated as the applied shear stress surplus the specified shear bond strength either by rotation or by shearing of particles. The tensile strength at the contact immediately drops to zero after the bond breaks, while the shear strength decreases to the residual friction value (Itasca Consulting Group Inc 2004; Cho et al. 2007, 2008; Potyondy and Cundall 2004). For all these microscopic behaviors, PFC only requires selection of the basic micro-parameters to describe contact and bond stiffness, bond strength and contact friction, but these micro-parameters should provide the macro-scale behavior of the material being modeled. The code uses an explicit finite difference scheme to solve the equation of force and motion, and hence one can readily track initiation and propagation of bond breakage (fracture formation) through the system (Potyondy and Cundall 2004). In addition, the user can track the failure process at each contact and determine if the dominant mode of failure is either tensile or shear.

One of the requirements for the bonded particle model (BPM) is the calibration of the micro-contact parameters to match the macro-scale response. While the approach and benefits of the BPM are compelling, but it is not clear if the calibration of the BPM to a uniaxial test is adequate for modeling any problem in that material. Although Diederichs (2002) showed that one of the disconcerting results is that the uniaxial compressive strength obtained in PFC is approximately four of the tensile strength. Based on this finding, the ratio of uniaxial compressive strength to tensile strength of fabricated synthetic rock-like material was chosen equal to 5.5 for satisfying a nearly good consistency between numerical and experimental results. Potyondy and Cundall (2004) also demonstrated that a non-ideal triaxial

Fig. 2 **a** The schematic view of ligament length, **b** photograph of shear testing machine



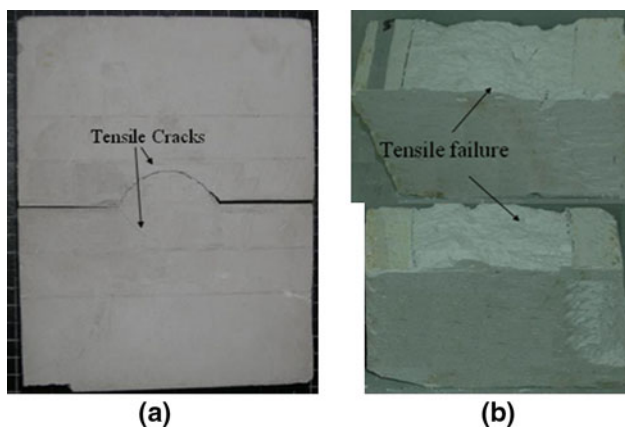


Fig. 3 The crack patterns for different ligament angles; **a** ligament length = 45 mm, **b** ligament length = 90 mm

envelope is obtained if calibration is performed with uniaxial strength of high-friction angled crystalline rock. Hence, the particles in both laboratory synthetic rock and numerical model were chosen to be circular and low friction angle (equal to 20.4°).

3.1 Preparation and Calibration of the PFC2D Model for Rock-Like Material

The standard process of generating a PFC2D assembly to represent a test model, used in this article, is described in detail by Itasca (2004). The process involves: particle generation, packing the particles, isotropic stress installation (stress initialization), floating particle (floater) elimination and bond installation. A gravity effect did not need to be considered as the specimens were small, and the gravity-induced stress gradient had a negligible effect on the macroscopic behavior.

Uniaxial compressive strength, Brazilian and biaxial tests were carried out to calibrate the properties of particles and parallel bonds in bonded particle model.

The applied loading rate in each test should be set sufficiently slow enough to ensure that the force, displacement, velocity and acceleration should not propagate from any particle farther than its immediate neighbors during a single time step. Under the low loading rate, the sample remains in a quasi-static equilibrium throughout the test and is stable so as not to induce any possible strength increase or unexpected material responses within the simulated models.

Figure 4a shows the effect of the loading rate on the stress–strain curve. The mechanical responses of test samples of 14,298 particles are clearly dependent on the loading rate in the elastic range of the particle material. An oscillatory behavior in the stress–strain curve is observed if the loading rate is of 0.4 m/s. On the other hand, the oscillatory behavior of the mechanical response is greatly reduced when a smaller loading rate (i.e., 0.016 m/s) is applied.

Figure 4b exhibits the effect of the loading rate on both of uniaxial strength and Brazilian tensile strength of numerical models. As it can be seen, the loading rate of ‘0.016 m/s’ is the upper limit of the loading rate that can be imposed on loading for compressive and tensile strength tests, whereas the effect of the loading rate was shown to be consistent for lower values. Hence, the loading rate adopted in this study was chosen to be 0.016 m/s.

Adopting the micro-properties listed in Table 2 and the standard calibration procedures (Potyondy and Cundall 2004), a calibrated PFC particle assembly was created.

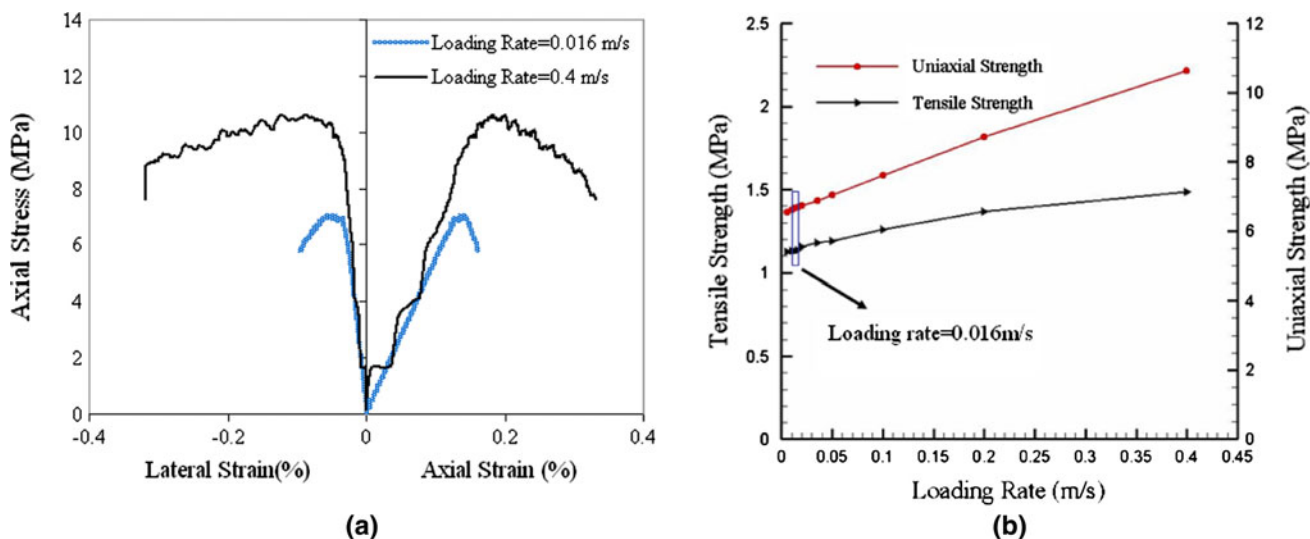


Fig. 4 The effect of the loading rate on the **a** curve of axial stress versus axial strain, **b** mechanical properties of numerical model

Table 2 Micro properties used to represent the intact rock

Parameter	Value	Parameter	Value
Type of particle	Disc	Parallel-bond radius multiplier	1
Density (kg/m ³)	1,000	Young's modulus of parallel bond (GPa)	4
Minimum radius (mm)	0.27	Parallel bond stiffness ratio	1.7
Size ratio	1.56	Particle friction coefficient	0.4
Porosity ratio	0.08	Parallel bond normal strength, mean (MPa)	5.6
Damping coefficient	0.7	Parallel bond normal strength, SD (MPa)	1.4
Contact Young's modulus (GPa)	4	Parallel bond shear strength, mean (MPa)	5.6
Stiffness ratio	1.7	Parallel bond shear strength, SD (MPa)	1.4

The specifications of different numerical tests considered for model calibration are summarized in the following sections:

3.1.1 Numerical Unconfined Compressive Test

In PFC2D, the uniaxial compression test can be simplified to a model of two moving walls compressing the particle assembly as illustrated in Fig. 5 with lines indicating the break of bonds and where the micro-cracks can be found. The black and the red lines represent the tensile failure and the shear failure, respectively. The walls were selected to be frictionless rigid plates. The tested specimen of assembly is 108 mm in height and 54 mm in width, and consists of 14,298 particles. A normal particle size distribution was used, with particle radii ranging from 0.27 to 0.4212 mm. The bounds of the particle radii were chosen so as to have particles that are as small as possible, without compromising computational efficiency, and minimizing code running time. The porosity ratio was chosen as 0.08, which is a reasonable value for a dense packing. The modulus E , Poisson's ratio, crack initiation stress and uniaxial compression strength (UCS) of the particle assembly can be obtained through the PFC2D simulation. The procedure to determine these parameters has been described elsewhere (Itasca Consulting Group Inc 2004).

Figure 6 compares the stress-strain curves respectively obtained by experiment and by numerical simulation. It can be seen that these two curves shown in Fig. 6 are consistent in general, and the peak strength is also similar. Similar to the rock-like material as shown in Fig. 6, the bonded-particle model fractures at peak strength, followed by a substantial drop of resisting stress after peak; such behavior represents a typical brittle fracture. After the peak, a major, inclined fracture surface formed in the specimen upon subsequent loading (Fig. 5), and eventually the original intact specimen was broken apart. This fracture pattern is also similar to the rock-like material.

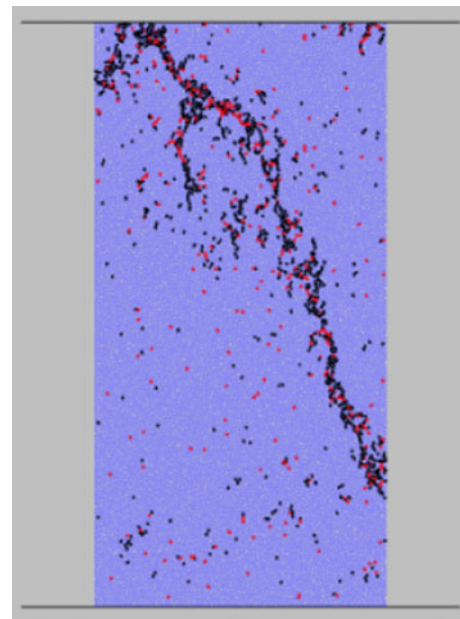


Fig. 5 Unconfined compressive test (cracks described by red/black lines)

A comparison of the numerical results with the experimental measurements is presented in Table 3.

3.1.2 Brazilian Test

Brazilian test was used to calibrate the tensile strength of the specimen in PFC2D model. The diameter of the Brazilian disk considered in the numerical tests was 54 mm. The specimen was made of 5,615 particles. The disk was crushed by the lateral walls moved toward each other with a low speed of 0.016 m/s. The numerical simulation is demonstrated in Fig. 7a through the variation of tensile stress versus axial displacement. It is evident, from the figure, that the bonded particles have a brittle behavior under indirect tensile loading. Figure 7b, c illustrate the failure patterns of the numerical and experimental tested samples, respectively. The failure planes experienced in numerical and laboratory tests are well matching. The

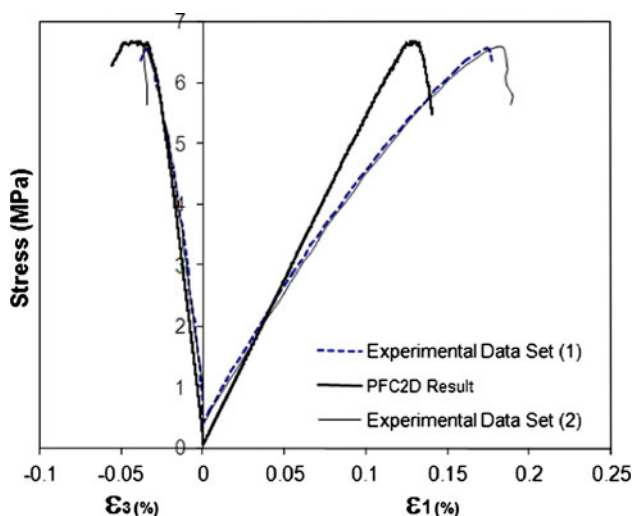


Fig. 6 The stress–strain curves obtained by experiment and by numerical simulation

numerical tensile strength and a comparison of its experimental measurements are presented in Table 3.

3.1.3 Biaxial Test

The specifications of the tested specimen in biaxial test (or more generally known as tri-axial test as $\sigma_2 = \sigma_3$) are the same as those given for the uniaxial test. For biaxial testing, the rectangle model is loaded appropriately by the surrounding four walls. The confined and vertical stresses are applied to the specimen by activating the servo-mechanism that controls the velocities of the four confined walls. Figure 8 depicts the strength envelope for the laboratory-tested material and also of the PFC model. It can be seen that the numerical testing matches the experimental well.

A comparison of these experimental results given in Table 3 demonstrates suitably good agreement with those of the numerical measurements.

3.2 Numerical Direct Shear Tests on the Non-Persistent Open Joint

3.2.1 Preparing the Model

After calibration of PFC2D, direct shear tests for jointed rock were numerically simulated by creating a shear box model in

the PFC2D (by using the calibrated micro-parameters) (Fig. 9). The PFC specimen had the dimensions of 76×60 mm. These dimensions are chosen as 40 percent (40 %) less than the laboratory synthetic sample dimensions to reduce the code running time. A total of 11,179 disks with a minimum radius of 0.27 mm were used to make up the shear box specimen. The particles were surrounded by four walls. The planar non-persistent joints were formed by deletion of two non-persistent vertical bands of particles from the model. The opening of these notches is 1 mm (Fig. 9). To create the shear test condition, two horizontal narrow bands of particles, with the width of 1 mm, were deleted from both the upper left side and the lower right side of the model at a distance between the joint walls and the shear box wall (Fig. 9).

In total four specimens containing two planar edge-notched joints with different lengths were set up to investigate the influence of joint separation on the shear behavior of rock bridges. For different specimens, the lengths of these edge-notched joints were different, while in the same specimen, the lengths of those two joints were the same, and they are both arrayed in the vertical middle plane. The joint length (b) has a range from 12 to 25.5 mm with an increment of 4.5 mm, while the joint separation or ligament length (l) decreases from 36 to 9 mm with a negative change value of 9 mm. Based on the change in the length of planar non-persistent joints, it is possible to define the joint coefficient (JC) as the ratio of the joint length to the total shear length, i.e., $2b/(l + 2b)$. The value of JC increases from 0.4 to 0.85 with an increment of 0.15.

3.2.2 Loading Set Up

Both the upper and left walls of the shear box were fixed (Fig. 9). Shear loading was applied to the sample by moving the lower wall in the positive Y -direction, with an adequate low velocity (i.e., 0.016 m/s) to ensure a quasi-static equilibrium, while the normal stress was kept constant by adjusting the right wall’s velocity using a numerical servo-mechanism. The normal stress applied to the rock bridges in the numerical tests was the same as in the laboratory tests (i.e., 0.33 MPa), which is approximately 5 % of the uniaxial strength of the intact sample. Shear displacement was measured by tracing the lower vertical wall displacement (Fig. 9, wall 1). The shear force was registered by taking the reaction forces on the wall 2 in Fig. 9.

Table 3 Macro-mechanical properties of the model material in the experimental tests and PFC2D

Mechanical properties	Experimental results	PFC2D model results	Mechanical properties	Experimental results	PFC2D model results
Elastic modulus (Gpa)	5	5	Tensile strength (MPa)	1	1.1
Poisson’s ratio	0.18	0.19	Friction angle	20.4	21
UCS (Mpa)	6.6	6.7	Cohesion (MPa)	2.2	2.2

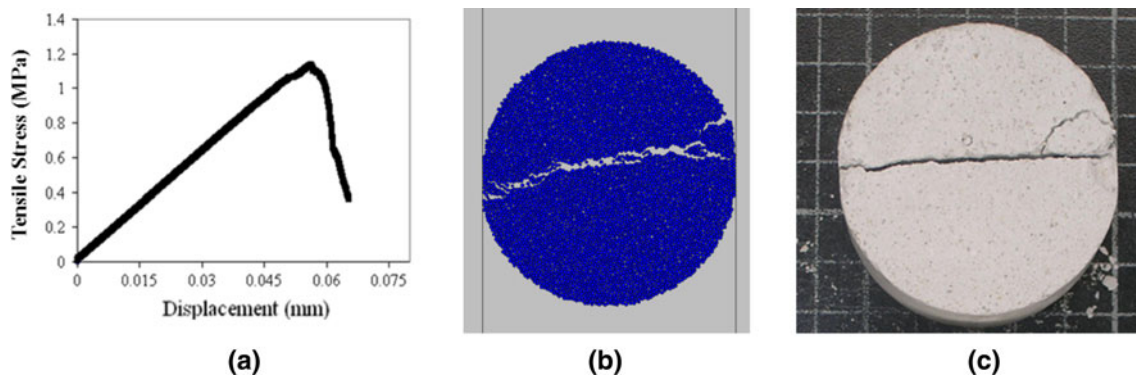


Fig. 7 **a** Tensile strength versus axial displacement curve for numerical Brazilian test simulation, **b** failure pattern in PFC2D model, **c** failure pattern in physical sample

An internal measurement circle installed at the center of the sample. The diameter of this measuring circle is equal to the ligament length (Fig. 9). The stress measurement circle was to evaluate how the average shear and normal stresses (σ_x and σ_y respectively) behave during the shear loading. Furthermore, it was used to evaluate the nature of the developed σ_x and σ_y at failure (tensile or compressive). Support of a PFC2D manual code was sought to measure the resulting contact force between the disks falling inside the circle. The average stress for the X or Y axis is a ratio of referred resulting contact force divided by the circle area.

4 Results and Discussion

4.1 Parallel Bond Forces in the Models Before Crack Initiation

Figure 10a, b shows the parallel bond force distribution at a state before the crack initiation in two PFC samples, which have the lowest and highest value of JC (0.4 and 0.85), respectively. The dark and red lines represent the compression and tensile forces in the model, respectively. The coarser the line is, the larger the force is. As can be seen, the maximum force concentrations occur around the joint tips.

For example, when the joint coefficient was 0.85 (Fig. 10b), the maximum compressive force on the crack tips was equal to 1,600 N. The maximum tensile force, developed near the tip of the joint, was equal to 1,289 N. As the tensile strength of the particles bonded at the tip of the joint was less than their shear strength, it can be concluded that the tensile crack is a dominant mode that initiates at the tip of the joint.

4.2 Contact Force and Displacement Distribution in the Models

Figure 11a, b shows the contact force distribution before the crack initiation in two PFC samples, which have the lowest and highest value of JC (0.4 and 0.85), respectively.

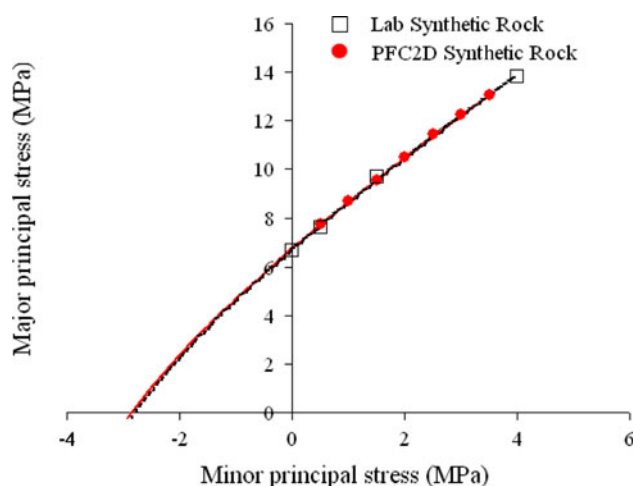


Fig. 8 Calibrated failure locus for PFC synthetic rock compared to the laboratory measured

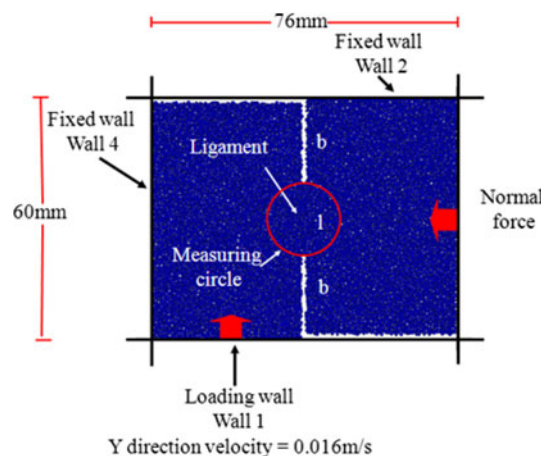


Fig. 9 Illustration of the direct shear test simulation scheme in PFC

Also shown in Fig. 11c is the typical contact force distribution in an intact model under direct shear loading reported by Cho et al. (2008).

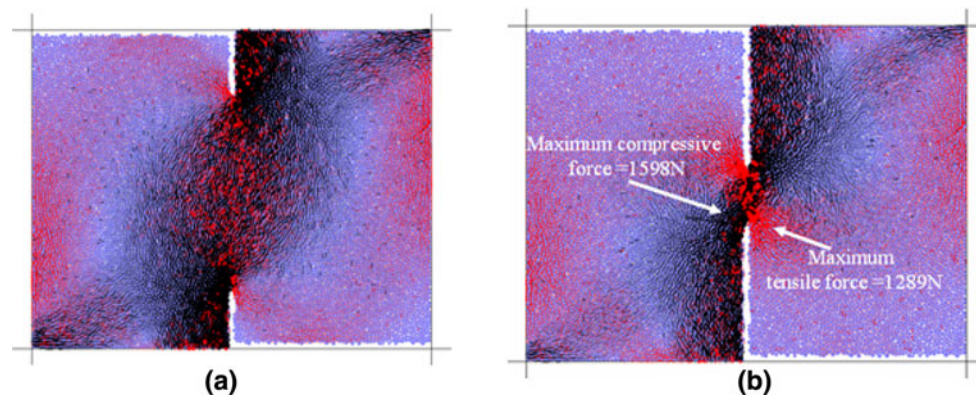


Fig. 10 The distribution of forces in the models before the crack initiation occurs; **a** $JC = 0.4$ and **b** $JC = 0.85$

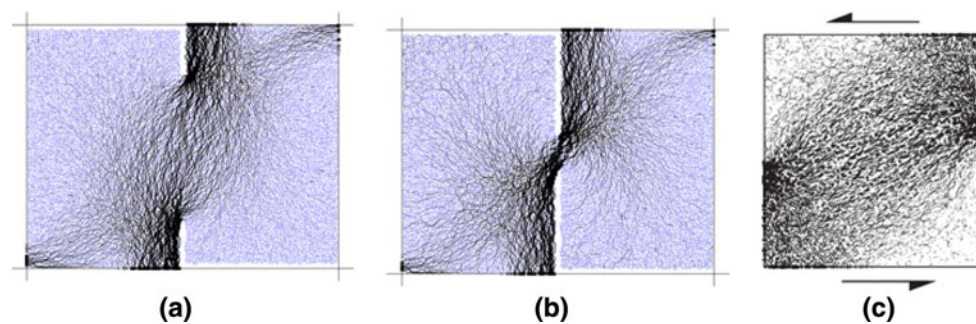


Fig. 11 The contact force distribution in PFC simulated models, **a** $JC = 0.4$, **b** $JC = 0.85$ and **c** the contact force distribution in intact PFC-simulated model, reported by Cho et al. (2008)

The lines are parallel to the contact forces, and the line thickness is proportional to the magnitude of the forces. It is clear that the contact forces in the samples are not uniformly distributed as the sample approaches the peak strength. In the intact model, the contact force concentration occurs near the center of the edges of the sample (Fig. 11c), while in the jointed models, the contact force is concentrated near the joint tips as a result of notch creation in the intact model. By increasing of the JC from 0.4 to 0.85, the large contact force is concentrated at the bridged part as a result of force interaction between the joints. The contact forces in the center of the samples are inclined by approximately 0° – 40° to the shearing direction.

Figure 12a, b shows the particle displacement vectors in two PFC samples, which have the lowest and highest value of JC (0.4 and 0.85), respectively. Also shown in Fig. 12c is the typical displacement vector observed in a Brazilian tensile test simulation using the same micro-parameters as in the direct shear test. The displacement vectors of the particles in a given PFC assembly illustrate how the particles are moving as they are subjected to the external loading conditions.

As shown in Fig. 12, despite the unique differences in the stress paths between the direct shear test and the Brazilian test, the displacement vectors show similar trends,

and the fractures display an opening phenomenon, characteristic of mode I fractures, i.e., the fracture mechanics terminology for fractures subjected to tensile loading.

4.3 Local Stress Path

Using the measurement circle described in Sect. 3.2.2, the stress path for the direct shear test can be tracked and expressed in the σ_x – σ_y space. Figure 13 shows the local stress path for two PFC samples, which have the lowest and highest value of JC (0.4 and 0.85), respectively.

At the beginning of external shear loading, rock bridges are subject to compressive loading (both of the σ_x and σ_y are positive). By increasing the external shear loading, the minimum principal stress changes from compression into extension (σ_x changes from positive into negative), so that tensile cracks are developed in the rock bridges.

4.4 Influence of Joint Separation on the Failure Behavior of the Rock Bridge

Figures 14, 15, 16 and 17 illustrate the fracture patterns recorded at each stage in the loading of the planar non-persistent joint for $JC = 0.15$, 0.3, 0.45 and 0.6,

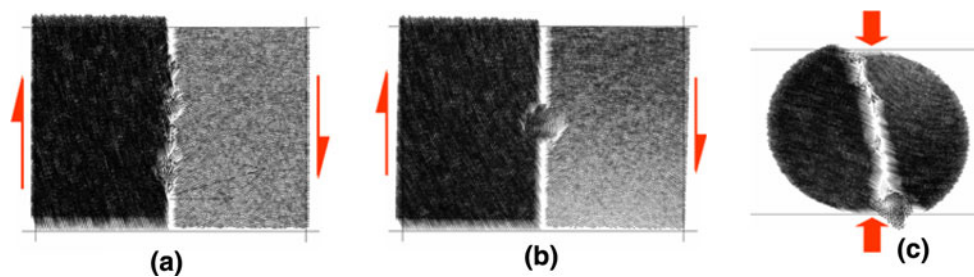


Fig. 12 Displacement vectors during the fracture development; **a** $JC = 0.4$, **b** $JC = 0.85$ and **c** the typical displacement vector observed in a Brazilian tensile test

respectively. In each case, the conditions at the three stages of fracture development (i.e., before the peak, at the peak and after the peak shear strength) were recorded. The black and red lines represent the tensile failure and the shear failure, respectively. At each stage of the simulation, the evolution of the bond force has been shown. The dark and red lines represent compression forces and tensile forces, respectively; the coarser the line, the bigger the force acting at the model. Also at each stage of the simulation, the crack orientation and the number of shear and tension induced cracks were determined. The approximate orientation of cracks was plotted in rose diagrams. The length of the orientation vector is associated with the number of micro cracks. The 0° axis in the rose diagram is aligned to the vertical axis in direct shear simulation, and all angles are measured counter-clockwise starting from the vertical axis. The mean orientations of the sketched fractures plotted on the rose diagram were classified into three distinct fracture sets. The first fracture set (F1) was taken from 40° to 90° , the second fracture set (F2) was taken from 0° to 40° , and the third fracture set (F3) was taken from 90° to 180° . These three fracture sets F1, F2 and F3 are marked in these figures with a black line, green line and red lines; respectively.

4.4.1 $JC = 0.85$

Stage A: As seen in Fig. 14a, before the peak shear stress is reached, only tensile fractures are initiated at the tip of the joints as a result of the release of tensile force. They propagate out of the maximum compressive force zone to form the so-called “wing cracks.” These cracks are categorized in the major fracture set of F1 with a mean orientation of 65.5° . After breakage of the bonds, the kinematic energy is released and transmitted into the neighboring bonds. Since the force intensity at the unbroken bonds is not enough to rupture the contacts, the cracks develop in a stable manner.

Stage B: As seen in Fig. 14b, when the shear stress reaches the peak strength, the new tensile cracks are developed along the fracture set of F1 and propagate out of the zone of maximum compressive force for a large distance.

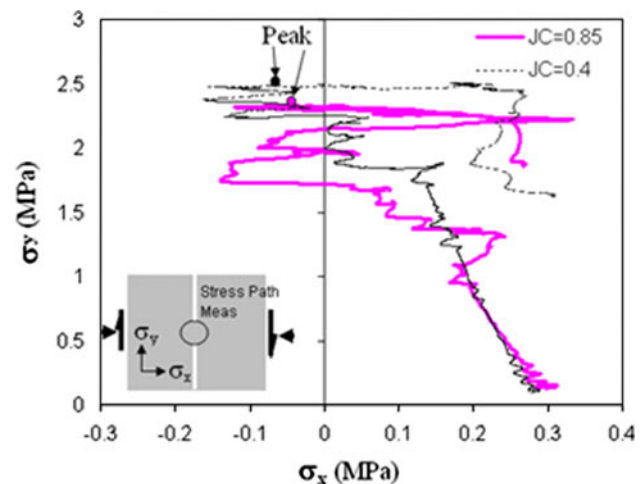


Fig. 13 Stress path measurement at the center of PFC model. The points marked by the *big arrow* correspond to the peak shear stress

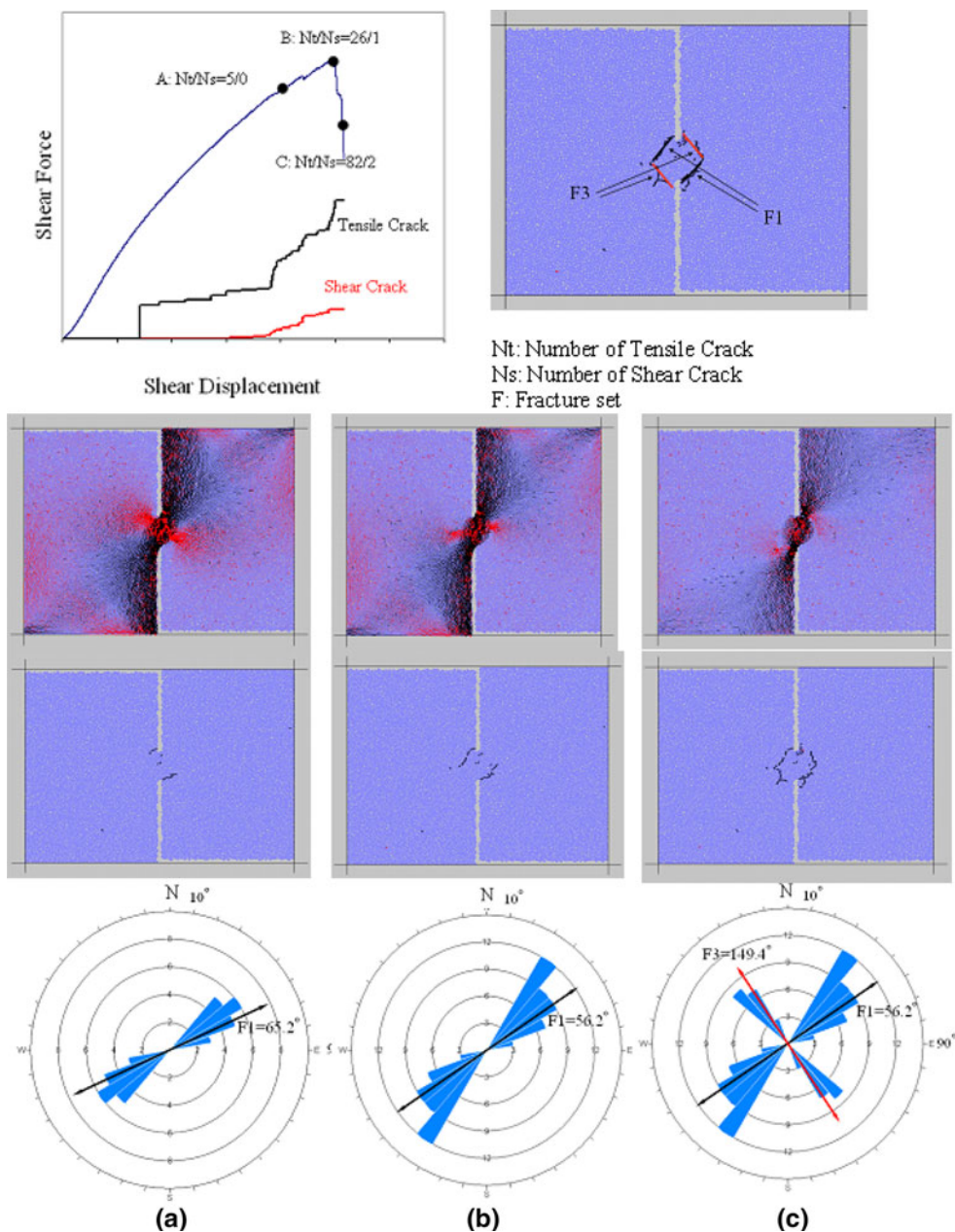
The mean orientation of the fracture set, F1, is 56.2° . After the bonds are broken, the maximum tensile force is concentrated near the broken bonds, while the maximum compressive force is distributed at the midst of rock bridge. By this force redistribution, we can predict that the latter breakages will occur in the vicinity of the broken bonds.

Stage C: In the final stage, as shown in Fig. 14c, a new tensile fracture set, F3, develops in the vicinity of the fracture set of F1 and propagates out of the zone of maximum compressive force till coalescence with the joint tip. This coalescence leaves an elliptical core of intact particles. The mean orientation of the two fracture sets of F1 and F3 is 56.2° and 149.4° , respectively. The force distribution at this stage shows that the compressive force chains have developed in the model and have taken an elliptical form at the middle part. The final failure occurs by breakage of these chains. It is worth noting that a few shear cracks are observed in the broken model as a result of breakage of shear bonds.

4.4.2 $JC = 0.7$

Stage A: As seen in Fig. 15a, the upper and lower tensile cracks (in the fracture set, F1) develop with a mean

Fig. 14 Development of cracks, evolution of the bond forces and mean orientation of particle cracks during the three stages of shear loading: **a** before peak, **b** at peak and **c** after peak shear strength, $JC = 0.85$



orientation of 48.8° from the notch tips prior to the peak shear stress being attained. These propagate out of the maximum compressive force zone for a considerable distance. Also, a few tensile cracks with the mean orientation of 27.8° (in the fracture set, F2) develop within the rock bridge. These fracture sets turn stable because of the release of tensile force with the development of tensile cracks.

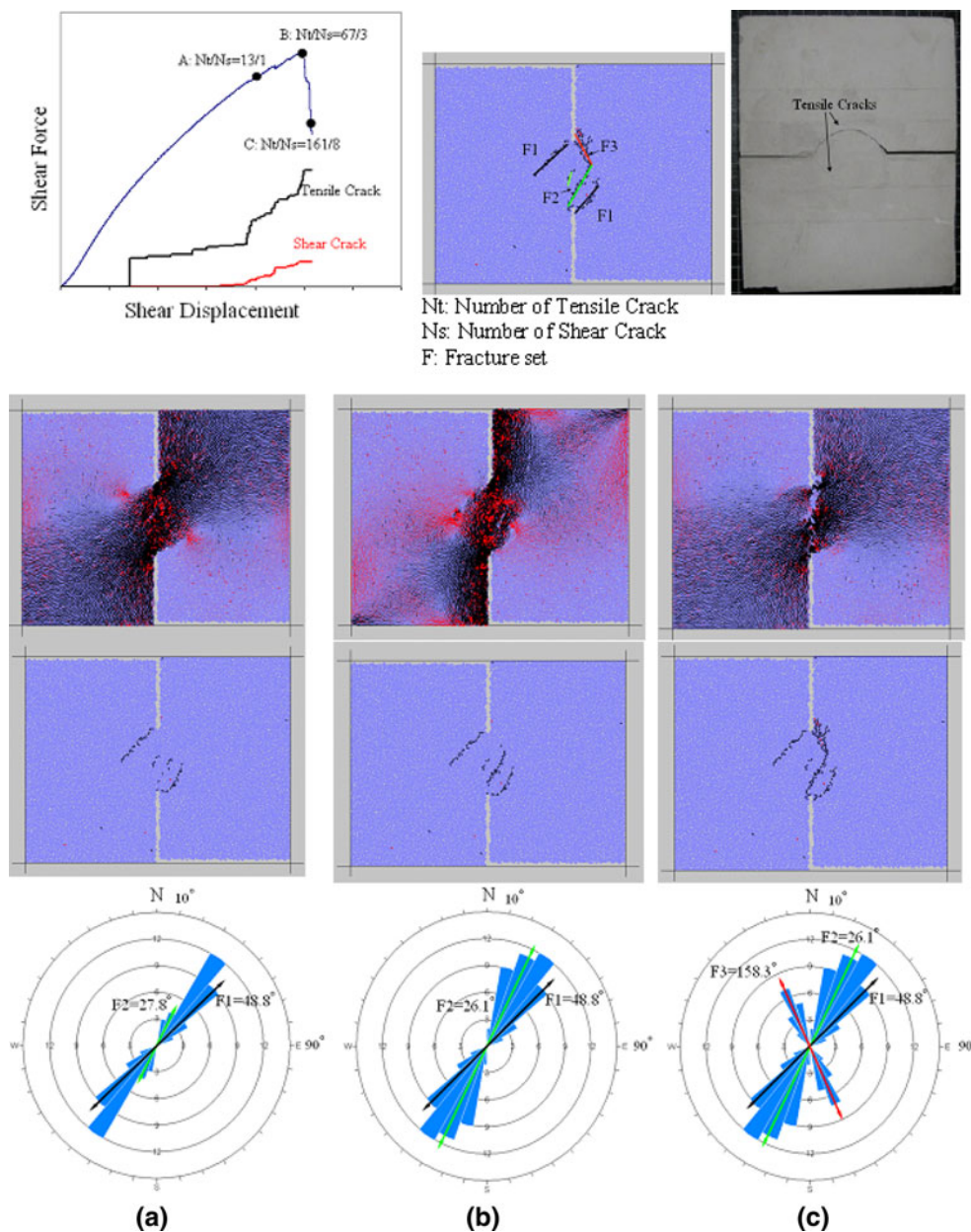
Following the bond breakage, the maximum tensile force is concentrated close to these two fracture sets.

Stage B: As the shear stress reaches the peak strength (Fig. 15b), the new tensile cracks that form the fracture set, F2, develop at the midst of the rock bridge and propagate

within the zone of maximum compressive force. Also some tensile cracks develop near the fracture set F1. The mean orientation of the two distinct fracture sets of F1 and F2 is 48.8° and 26.1° , respectively. In this stage, the number of newly developed tensile cracks existing in the fracture set F2 is more than that in the fracture set F1. This means that the maximum tensile force has been transmitted within the rock bridge. The force distribution in the rock bridge shows that the maximum tensile force is concentrated near the broken bond.

Stage C: In the final stage of the shear loading, as shown in Fig. 15c, tensile cracks develop near the fracture set, F2. Also the tensile fracture set F3 develops within the rock

Fig. 15 Development of cracks, evolution of the bond forces and mean orientation of particle cracks during the three stages of shear loading: **a** before peak, **b** at peak and **c** after peak shear strength, $JC = 0.7$



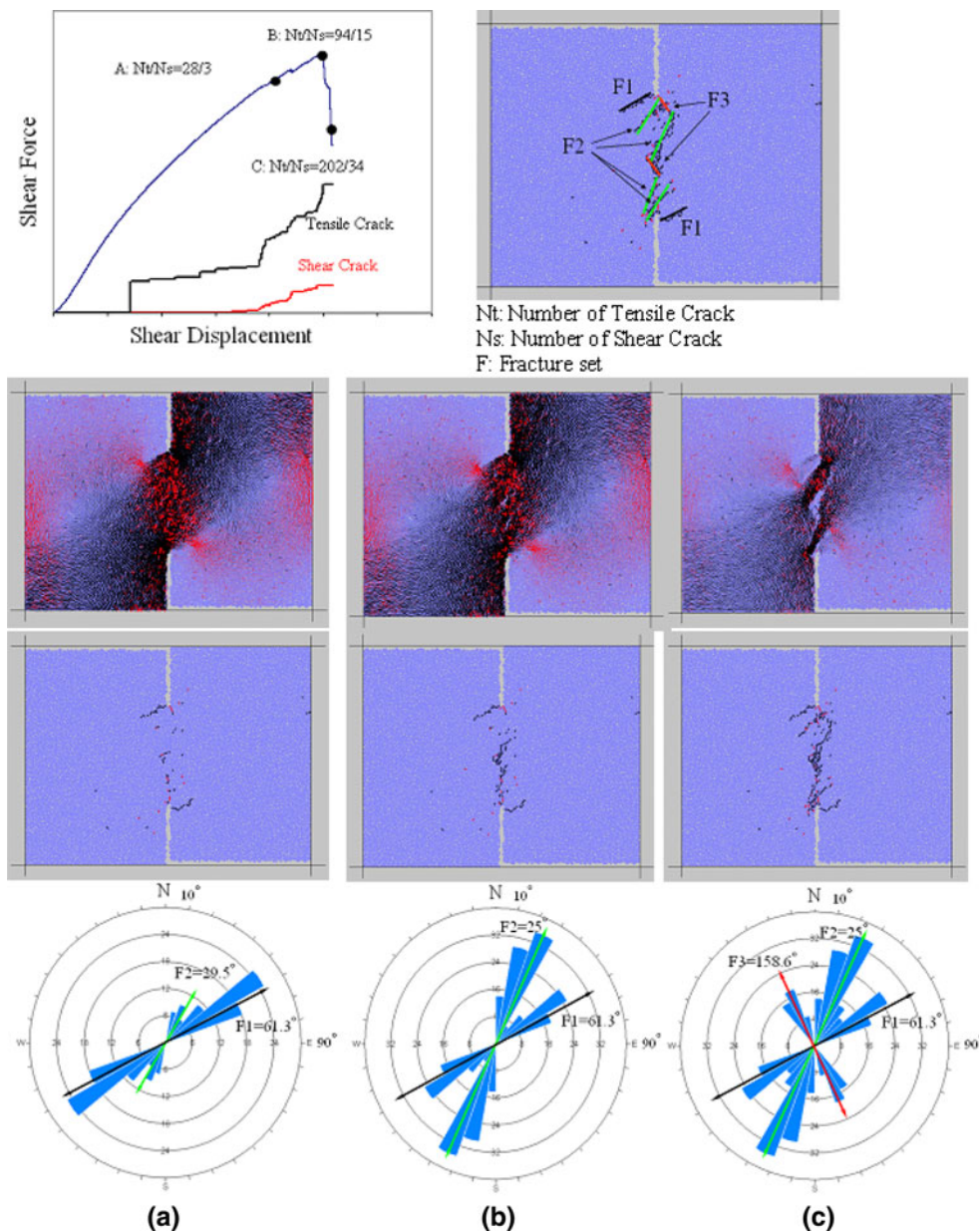
bridge and coalesces with the joint tip so that the intact bridge area gets split with an uneven shear failure surface. It is worth noting that a few shear cracks are observed in each fracture set. The mean orientation of two fracture sets, F1 and F3, is 26.1° and 158.3° , respectively. The length and orientation of fracture set F1 remain constant after the first stage. It means that the external shear load has no effect on the force concentration near the fracture set F1 after the first stage of shear loading. The bond force distribution at this stage shows that the force chains take an uneven form according to the geometry of the failure surface. These force chains are stable till the ultimate breakage occurs in the rock bridge. It is important to note that only two fracture sets of F2 and F3 are responsible for

breaking the rock bridge. As can be seen from Fig. 3a, nearly the same failure pattern has occurred in the physical sample when $JC = 0.7$.

4.4.3 $JC = 0.55$

Stage A: As shown in Fig. 16a, before the peak shear stress is reached, two distinct tensile fracture sets of F1 and F2 are identified in the bridge area with a mean orientation of 61.3° and 29.5° , respectively. The upper and lower tensile wing cracks (in fracture set, F1) develop at the notch tips and propagate out of the zone of maximum compressive force for a short distance. Also the fracture set of F2 develops at the midst of rock bridge as several short shear

Fig. 16 Development of cracks, evolution of the bond forces and mean orientation of particle cracks during the three stages of shear loading: **a** before peak, **b** at peak and **c** after peak shear strength, $JC = 0.55$



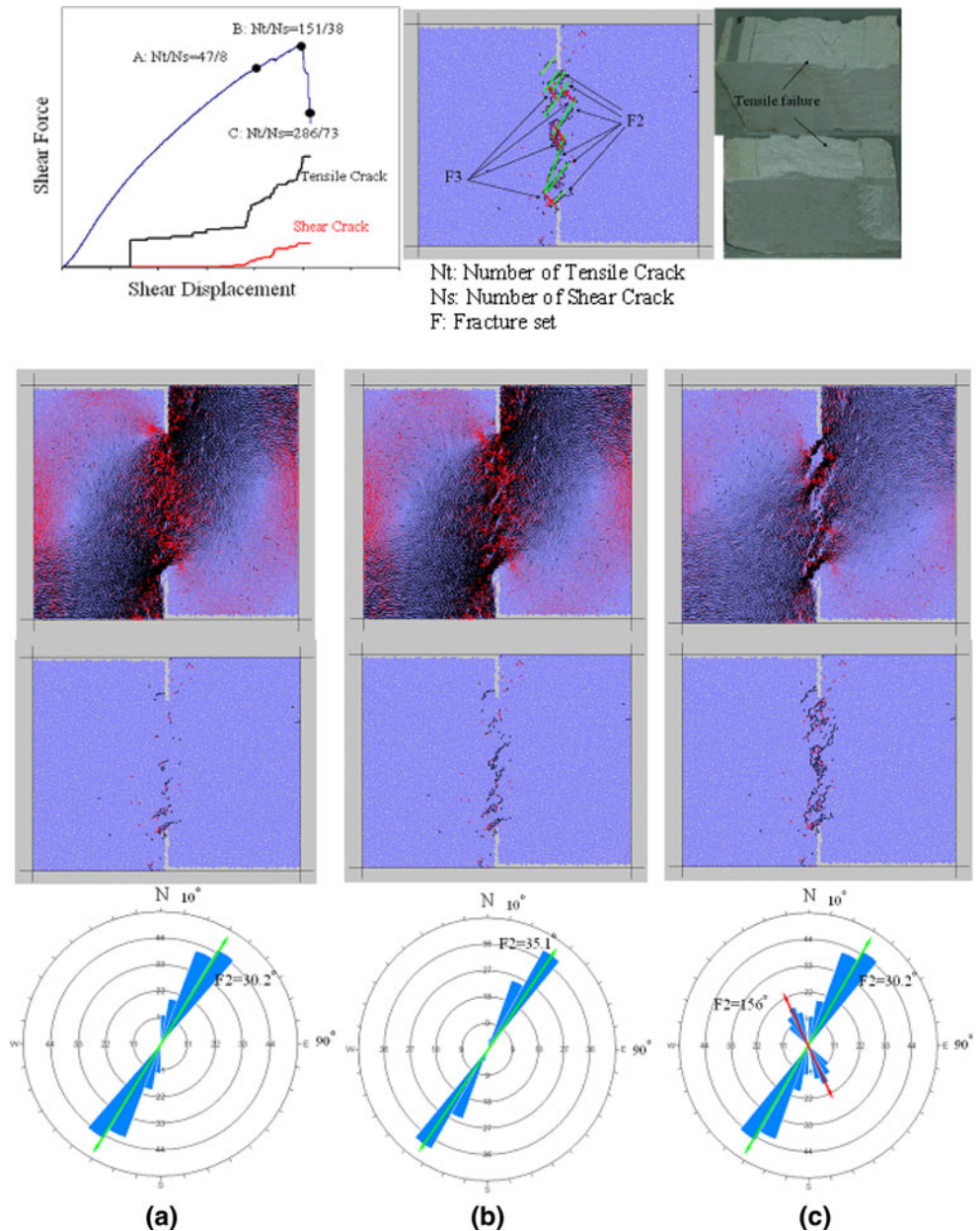
bands because of the low stress interaction between the joints. In other words, several short bands of contacts in the midst of the rock bridge that are weak due to their critical situation related to the shear loading path (about $0^\circ\text{--}40^\circ$), break simultaneously with crack initiation at the tip of the joints. These two fracture sets propagate for a short distance and become stable due to the development of tensile cracks. Note that the direction of weak bands is in a good agreement with the contact force distribution in the center of the samples, which are inclined by approximately $0^\circ\text{--}40^\circ$ to the shearing direction (Fig. 11).

Stage B: As the shear stress reaches the peak strength (Fig. 16b), the new tensile cracks develop along the fracture set F2, so the shear bands propagate within the zone of

maximum compressive force for a large distance. The mean orientation of fracture set F2 is equal to 25° . Force redistribution in the midst zone shows that the high tensile force is concentrated in vicinity of the fracture set F2.

Stage C: In the final stage of the shear loading, as shown in Fig. 16c, the short tensile fracture set F3 develops between the shear bands so that the intact bridge area gets broken with an unsymmetrical shear failure surface. The mean orientation of fracture set F3 is 158.6° . It is important to note that only the two fracture sets of F2 and F3 are responsible for the breakage of the rock bridge. The length and orientation of fracture set F1 remain constant after the first stage of shear loading. It means that the external shear load does not induce any force concentration near the

Fig. 17 Development of cracks, evolution of bond forces and mean orientation of particle cracks during three stages of shear loading; **a** before peak, **b** at peak and **c** after peak shear strength, $JC = 0.4$



fracture set F1 during the different stages of shear loading (stages of B and C). The bond force distribution shows that the force chains develop within the unbroken parts of the rock bridge. These chains affect the post peak behavior of the shear surface till the final breakage of the bonded particles is reached. Note that the tensile cracks are the dominant mode of failure, while a few shear cracks develop within the model.

Wong et al. (1999, 2001) gained similar related results showing that ‘fish eye’ mode coalescence occurs in a critical range of joint coefficients ($JC = 0.55$) in experiments using plaster modeling material under direct shear tests.

4.4.4 $JC = 0.4$

Stage A: Figure 17a indicates that both shear and tensile cracks (in fracture set F2) accumulate in the rock bridge prior to the peak shear stress being attained. It can be seen that several shear bands propagate in a stable manner within the zone of maximum compressive force because of the low stress interaction between the joints. The mean orientation of the tensile fracture set F2 is 35.1° .

Unlike in the previous cases, there are no cracks at the tip of the joints in this stage. In other words, the stress concentration at the tip of the joints is not enough to overcome the bond strength, while several short bands of

contacts, due to their critical situation with respect to the shear loading path (about 0° – 40°), break in the rock bridge.

Bond force distribution shows that the maximum tensile force is concentrated near the fracture set F2.

Stage B: As the shear stress reaches the peak strength (Fig. 17b), new cracks (tensile/shear) develop along the fracture set F2 so the shear bands propagate within the zone of maximum compressive force for a large distance. The mean orientation of the tensile fracture set of F2 is 30.2° . The force redistribution in the middle zone shows that the maximum forces are concentrated near the shear bands.

Stage C: In the final stage of shear loading (Fig. 17c), the short fracture set of F3 consists of both shear and tensile cracks, with a mean orientation of 156° , and develops between the shear bands so that the intact bridge area gets broken with an unsymmetrical shear failure surface. The fracture set F3 is approximately symmetrical to the fracture set F2, but in the opposite direction. The bond force distribution shows that the force chains develop within the unbroken rock bridge. The existence of bond forces in the rock bridge affects the residual strength of the broken model. As shown in Fig. 3b, nearly the same failure pattern has occurred in the physical sample when $JC = 0.7$.

The failure pattern obtained from this simulation is in reasonable accordance with some of the related numerical results in Zhang et al. (2006).

The crack ratios shown in Figs. 14, 15, 16 and 17 clearly reveal that tension cracks are considerably greater in number than the shear cracks. Such differences become even more significant as shear deformation increases. Also, in all the tested samples, nearly 45 % of total crack numbers develop at the peak strength (stage B), and 55 % of them develop after the peak shear resistance is reached. It shows that the planar non-persistent joints lose their loading capacity when 45 % of the total cracks develop within the rock bridges. From the above discussions, we can conclude that:

- The fracture morphology in planar rock bridges at low normal load level (0.33 MPa) does not occur because of shear stresses, but rather from tensile stresses.
- Three different tensile fracture sets develop within the rock bridges. The fracture set F1 is observed before the peak shear stress (stage A in Figs. 14, 15), and the fracture set F2 mainly is observed as the shear stress reaches the peak strength (stage B in Figs. 14, 15, 16, 17). Finally, before the shear stress approaches the residual strength (stage C in Figs. 14, 15, 16, 17), the two fracture sets F1 and F2 become kinetically impossible, and the fracture set F3 develops in the rock bridge.
- The fracture set F1 initiates at the joints tip but the other two fractures sets of F2 and F3 develop within the rock bridge.

- The joint coefficient controls the type of fracture set within the rock bridge. When the joint coefficient is high, the stress interaction between the joints is so strong that the two fracture sets of F1 and F3 are responsible for the breakage of the rock bridge. By decreasing the joint coefficient, the stress interaction between the joints is decreased and consequently the two fractures sets of F2 and F3 break the rock bridge.
- By decreasing the joint coefficient, the propagation length of fracture set F1 decreases, while the number and length of the other two fractures sets of F2 and F3 increase. This is due to the transition of maximum bond forces from the joints tip to the bridge area.
- When the joint coefficient is high, the failure zone is relatively narrow and has a symmetrical pattern, resulting from the high tensile stress concentration at the tip of the joints as well as the high stress interaction between the joints (Figs. 14, 15).
- When the joint coefficient is low, the rupture surface is more complex and develops into a shear zone. This zone is relatively thick and has an unsymmetrical pattern. The more complex shear zone results from the non-uniform distribution of the localized regions of tensility in the rock bridge (Figs. 16, 17).

Figure 18a illustrates the relationship between the shear load and shear displacement, and Fig. 18b represents the linear fitting curve of peak shear load and joint coefficient. Figure 18c shows the variation of failure stress of the bridged segment versus the joint coefficient for both the numerical and physical models. The fill points and hollow points represent the failure stresses in the PFC2D models and laboratory samples, respectively. The failure stress is measured by division of the maximum shear force by the length of the ligament.

Through comparison between Figs. 14, 15, 16, 17 and 18a, we can conclude that the peak of shear load is associated with the propagation length of the shear failure zone. The larger the propagation length is, the higher will be the peak of shear load.

The capacity of bridged rock to resist shear loading has a close relationship with the failure patterns. For a smaller joint separation ($JC = 0.85$), the intact-bridged rock ruptures in elliptical mode with two short strias; for a larger joint separation ($JC = 0.7$), tensile cracks propagate for a certain length and remain stable owing to the release of tensile stress. When the shear load increases, the middle bridged rock ruptures with a single uneven shear failure surface. For a larger joint separation ($JC = 0.55$), two joints are connected with several small shear bands. Finally, for the largest joint separation ($JC = 0.4$), a more complex shear zone, consisting of a large number of shear bands, propagates for a large distance and forms the final fracture surface. Also from

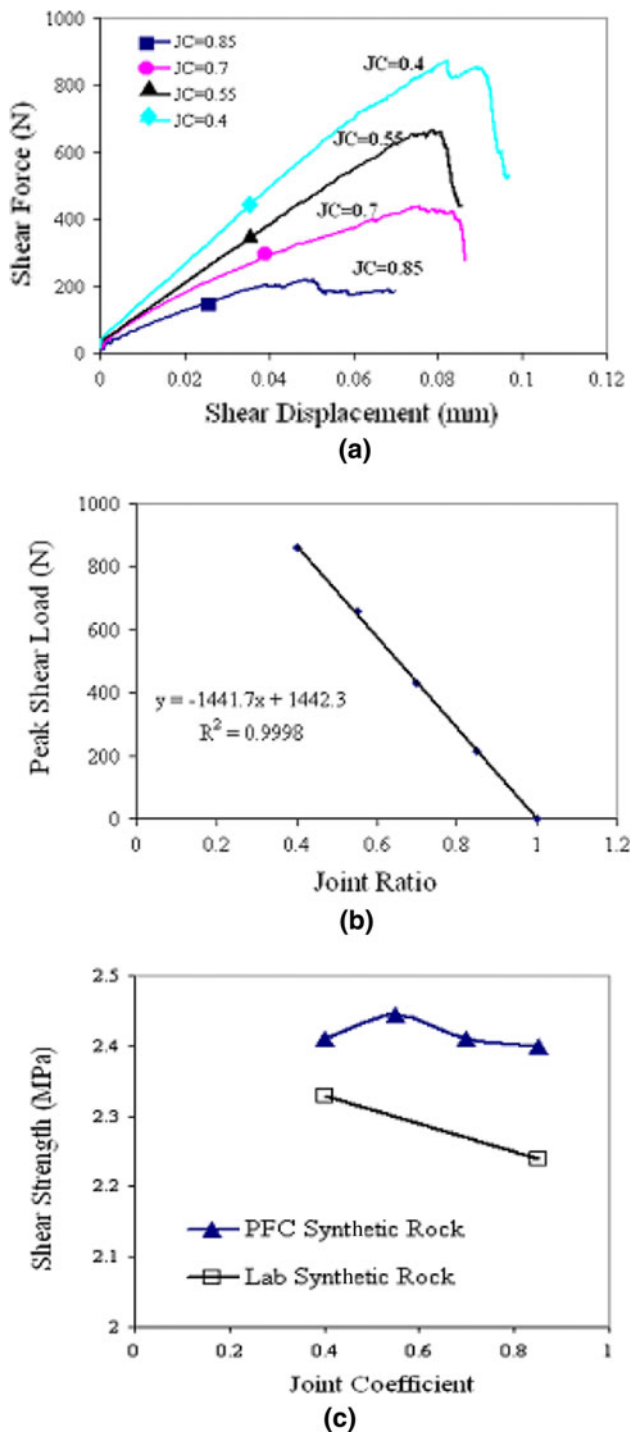


Fig. 18 a The relationship between the shear load and shear displacement. b The linear fitting curve of the peak of shear load and joint coefficient. c The variation of failure stress of the bridged segment versus the ligament angle

Fig. 18a, it is clear that the shear stiffness increases with decreasing the joint coefficient.

The linear fitting curve between the peak of the shear load and joint co-efficient in Fig. 18b shows that the peak of shear load is almost linear to the joint coefficient. The

smaller the ratio ($JC = 0.4$), the higher the peak shear load is. Note that the increase in the loading capacity of the rock bridge is not only due to the increase in the length of rock bridge. This may also be explained by the fracture mechanics theory, which indicates that small joint lengths correspond to small values of the stress intensity factors (KI and KII). This leads to higher rock bridge strength. From the fitting equation, $y = -1441.7x + 1442.3$ (Fig. 18b), it can be inferred that when the specimen has no pre-existing joints, the joint coefficient equals 0, and the peak of shear load is 1,442.3 N. The shear load would be 0.6 N (approximately close to 0) when the ideal condition is achieved [i.e., when the joint runs through the whole specimen ($JC = 1$)]. Therefore, the numerical results comply reasonably with the engineering expectation.

Figure 18c shows that the shear strength of non-persistent joints predicted by numerical simulations are nearly similar to the results obtained by experimental tests. The slight discrepancy may be due to some small variations in the mechanical specifications of numerical and laboratory specimens (i.e., the tensile strength and friction angle given in Table 3).

From Fig. 13c it is clear that the rock bridge capacity to resist shear loading has a close correlation (inversely proportional) with the joint coefficient. By increasing the joint coefficient, the shear strength of the rock bridge is reduced because of an increase in the stress concentration at the tip of the joints and an increase in the stress interaction between the joints.

Similarly, it may be concluded that the peak of shear load of jointed rock is mostly influenced by its failure pattern, while the failure pattern of bridged rock is mainly controlled by the joint separation.

Whereas shear strength, as one of the material mechanical properties, has a close relationship with its defect configuration, the capacity of jointed rock masses to resist shear loading is severely influenced by its macroscopic joint constellation.

5 Conclusion

The shear behavior (failure progress, failure pattern, failure mechanism and shear resistance) of rock specimens containing two edge joints with different joint separations was investigated with the direct shear test by PFC2D Numerical Simulation and verified by experimental tests. Based on the results obtained, the following conclusions drawn from this research are:

- By increasing the joint coefficient, the high fracture surface changes into a single symmetrical failure surface.

- Tension is the dominant mode of fracturing, irrespective of the stage of shearing.
- In all examined cases, about 45 % of the total number of cracks developed at the peak strength, and nearly 55 % of them developed after the peak shear resistance was reached. This revealed that the models lose their loading capacity when 45 % of the total number of cracks develops within the rock bridge.

Acknowledgment The support received from the Graz University of Technology, Graz, Austria, is thankfully acknowledged.

References

- Bobet A, Einstein HH (1998) Fracture coalescence in rock-type materials under uniaxial and biaxial compression. *Int J Rock Mech Min Sci* 35:863–888
- Cho N, Martin CD, Sego DC (2007) A clumped particle model for rock. *Int J Rock Mech Min Sci* 44:997–1010
- Cho N, Martin CD, Sego DC (2008) Development of a shear zone in brittle rock subjected to direct shear. *Int J Rock Mech Min Sci* 45:1335–1346
- Cundall P (1971) A computer model for simulating progressive large scale movements in blocky rock systems. In: Proceedings of the symposium of international society of rock mechanics, vol 1. Nancy, France. Paper no. II-8
- Diederichs MS (2002) Stress induced accumulation and implications for hard rock engineering. In: Hammah R, Bawden WF, Curran J, Telesnicki M (eds). *Proc NARMS*. University Toronto Press, pp 3–14
- Einstein HH, Veneziano D, Baecher GB, O'Reilly KJ (1983) The effect of discontinuity persistence on rock slope stability. *Int J Rock Mech Min Sci Geomech Abstr* 20(5):227–236
- Fakhimi A, Carvalho F, Ishida T, Labuz JF (2002) Simulation of failure around a circular opening in rock. *Int J Rock Mech Min Sci* 39:507–515
- Ghazvinian A, Nikudel MR, Sarfarazi V (2007) Effect of rock bridge continuity and area on shear behavior of joints. In: 11th congress of the international society for rock mechanics, Lisbon, Portugal
- Glynn EF, Veneziano D, Einstein HH (1978) The probabilistic model for shearing resistance of jointed rock. In: Proceedings of the 19th US symposium on rock mechanics, Stateline, Nevada, pp 66–76
- Hentz S, Daudeville L, Donze F (2004) Identification and validation of a discrete element model for concrete. *J Eng Mech* 130(6): 709–719
- Itasca Consulting Group Inc (2004) Particle flow code in 2-dimensions (PFC2D), Version 3.10, Minneapolis
- Lajtai EZ (1969a) Strength of discontinuous rocks in direct shear. *Geotechnique* 19:218–332
- Lajtai EZ (1969b) Shear strength of weakness planes in rock. *Int J Rock Mech Min Sci* 6:499–515
- Potyondy DO, Cundall PA (2004) A bonded-particle model for rock. *Int J Rock Mech Min Sci* 41(8):1329–1364
- Scavia C (1999) The displacement discontinuity method for the analysis of rock structures: a fracture mechanic. In: Aliabadi MH (ed) *Fracture of Rock*. WIT press, Computational Mechanics Publications, Boston, pp 39–82
- Scavia C, Castelli M (1996) In: Barla G (ed) *Analysis of the propagation of natural discontinuities in rock bridges*, EUROCK'98. Balkema, Rotterdam, pp 445–451
- Tang CA, Yang WT, Fu YF, Xu XH (1998) A new approach to numerical method of modelling geological processes and rock engineering problems-continuum to discontinuum and linearity to nonlinearity. *Eng Geol* 49:207–214
- Vasarhelyi B, Bobet A (2000) Modeling of crack initiation, propagation and coalescence in uniaxial compression. *Rock Mech Rock Eng* 33(2):119–139
- Wang C, Tannant DD (2004) Rock fracture around a highly stressed tunnel and the impact of a thin tunnel liner for ground control. *Int J Rock Mech Min Sci* 41:676–683
- Wong RHC, Chau KT (1998) Crack coalescence in rock-like material containing two cracks. *Int J Rock Mech Min Sci* 35:147–164
- Wong RHC, Chau KT, Tsoi PM, Tang CA (1999) Pattern of coalescence of rock bridge between two joints under shear testing. In: Vouile G, Berest P (eds). *The 9th international congress on rock mechanics*, Paris, pp 735–738
- Wong RHC, Leung WL, Wang SW (2001) Shear strength study on rock-like models containing arrayed open joints. In: Elsworth D, Tinucci JP, Heasley KA (eds) *Rock mechanics in the national interest*. Swets & Zeitlinger Lisse, The Netherland, pp 843–9 (ISBN:90-2651-827-7)
- Yoon J (2004) Application of experimental design and optimization to PFC model calibration in uniaxial compression simulation. *Int J Rock Mech Min Sci* 44:871–889
- Zhang HQ, Zhao ZY, Tang CA, Song L (2006) Numerical study of shear behavior of intermittent rock joints with different geometrical parameters. *Int J Rock Mech Min Sci* 43:802–816